Research Article | Vol. 11, No. 8 / 1 August 2020 / Biomedical Optics Express 4276
Biomedical Optics EXPRESS

Pathological identification of brain tumors based on the characteristics of molecular fragments generated by laser ablation combined with a spiking neural network

GEER TENG,[1,2] QIANQIAN WANG,[1,2,*] HAIFENG YANG,[3] XUELING QI,[4] HONGWEI ZHANG,[4] XUTAI CUI,[1,2] BUSHRA SANA IDREES,[1,2] WENTING XIANGLI,[1,2] KAI WEI,[1,2] AND M. NOUMAN KHAN[1,2]

[1]*School of Optics and Photonics, Beijing Institute of Technology, Beijing, 100081, China*
[2]*Key Laboratory of Photonic Information Technology, Ministry of Industry and Information Technology, Beijing Institute of Technology, Beijing, 100081, China*
[3]*Department of Neurosurgery, Kunming Sanbo Brain Hospital, Kunming, 650010, China*
[4]*Department of Neurosurgery, Beijing Sanbo Brain Hospital, Capital Medical University, Beijing, 100093, China*
[*]*qqwang@bit.edu.cn*

Abstract: Quick and accurate diagnosis helps shorten intraoperative waiting time and make a correct plan for the brain tumor resection. The common cryostat section method costs more than 10 minutes and the diagnostic accuracy depends on the sliced and frozen process and the experience of the pathologist. We propose the use of molecular fragment spectra (MFS) in laser-induced breakdown spectroscopy (LIBS) to identify different brain tumors. Formation mechanisms of MFS detected from brain tumors could be generalized into 3 categories, for instance, combination, reorganization and break. Four kinds of brain tumors (glioma, meningioma, hemangiopericytoma, and craniopharyngioma) from different patients were used as investigated samples. The spiking neural network (SNN) classifier was proposed to combine with the MFS (MFS-SNN) for the identification of brain tumors. SNN performed better than conventional machine learning methods for the analysis of similar and limited MFS information. With the ratio data type, the identification accuracy achieved 88.62% in 2 seconds.

1. Introduction

According to statistics, there were more than 18 million new cancer cases and 9.6 million cancer deaths worldwide in 2018 [1]. For most kinds of cancers, removing the tumor by surgery is the most effective treatment method. During the surgery, intraoperative pathological diagnosis will directly affect the next surgical plan. Especially for neurosurgery, accurate and fast pathological diagnosis of the brain tumor plays an important role. The intraoperative environment is significantly different from the intracranial environment during preoperative imaging detection, for instance, Magnetic Resonance Imaging (MRI) [2]. Therefore, tumor types and boundaries need to be determined intraoperatively. Meanwhile, due to the particularity of the disease site, clinical doctors cannot perform a biopsy diagnosis before surgery. The timeliness and accuracy of intraoperative tumor classification will directly affect the progress of the subsequent surgery. The intraoperative pathological diagnosis includes discrimination of benign and malignant tissues and discrimination of tumor types [3].

As a common intraoperative biopsy method, cryostat section method has been used for discrimination of tumor types and boundary tissues clinically [4]. Compared with paraffin

#397268 https://doi.org/10.1364/BOE.397268
Journal © 2020 Received 8 May 2020; revised 14 Jun 2020; accepted 7 Jul 2020; published 13 Jul 2020

Biomedical Optics EXPRESS

sections, the diagnosis based on cryostat section is faster and used as intraoperative standard. However, at present, it still takes 10 minutes to 15 minutes from material collection to section sealing for the leading frozen technology, and the diagnostic accuracy is not high enough [5]. According to the experience of clinical doctors, the cryostat section diagnostic accuracy is around 70% to 80%, which is influenced by the pathologist's experience. Therefore, a rapidly and accurately diagnostic technique needs to be developed for intraoperative detection.

Within the last decade, several histopathological diagnosis techniques based on tumor molecular biomarkers have been developed. For instance, Wright et al. found that 29 small molecule metabolites and 8 macromolecule signals detected by high-resolution magic angle spinning (HRMAS) NMR spectroscopy can be used as biomarkers for brain tumor classification [6]. Denkert et al. pointed to GC-TOF-based metabolomics as a new method for molecular pathology investigations [7]. Meanwhile, CircRNAs have been recognized as novel diagnostic and prognostic targets in tumors, especially in glioma [8]. Some autoantibodies have also been proved that they have potential application for cancer diagnosis [9]. However, previous works failed to address the speed of diagnosis. Many macromolecular differences in tumors can be used as molecular markers to diagnose tumors [10,11], but they are more suitable for postoperative research on pathogenesis. Intraoperative molecular diagnosis based on mentioned techniques requires a long time.

Focused on this problem, several quick detection methods have been proposed to diagnose the tissue classifications and characteristics during surgery, for instance, mass spectrometry [12,13], infrared spectroscopy [14], fluorescence [15] and Raman spectroscopy [16,17]. Eberlin et al. classified three kinds of brain tumors by desorption electrospray ionization-mass spectrometry (DESI-MS) imaging and 79% of tested features were consistent with the expert histopathology diagnosis [13]. The mass spectrometry equipment is expensive and complicated to maintain. During the detection, it often needs a partial vacuum environment. With recognized important spectral wavenumbers, Uckermann et al. achieved a high correct classification rate (CCR) at 88% through the Fourier-transform infrared spectroscopy [14]. However, infrared spectroscopy is not sensitive to water content in brain tissue, which is an obvious sign in some tumor tissues [18]. Desroches et al. used Raman spectroscopy to diagnose different kinds of brain tumors, but the sensitivity was only 80% [16]. Furthermore, only dense tumor tissue with more than 60% cancer cells can be diagnosed. In order to improve the accuracy, surface-enhanced Raman spectroscopy (SERS) was applied in cancer diagnosis [17]. The diagnostic accuracies of all developed techniques are still not high enough. The use of fluorescence or SERS technique requires to inject reagents, for example, the nanoparticles (NPs) reagents [15,17]. Residual reagents in the body may have influence on the nerve function, which makes the techniques cases with defects as intraoperative diagnostic methods. In general, current diagnostic techniques have not been able to diagnose various brain tumors quickly and accurately during surgery.

Previous works have been limited to identify macromolecules through biological or spectral methods. Few researchers have addressed the significance of molecular fragments in diagnosis of brain tumor. In this paper, we propose to use the molecular fragment spectra (MFS) in the laser-induced breakdown spectroscopy (LIBS) to distinguish different brain tumors. As a novel emission spectral technique, LIBS has been used for biological and medical detection field during the last decade [19,20]. The laser pulse is focused on biological tissue and interacted with the tissue material. Then, the trace amount of tissue is ablated and induced to generate plasma. During plasma cooling process, both atomic spectra (AS) and MFS can be collected. LIBS has played an important role in the diagnosis of different microorganisms and different types of tissues [21,22]. In the preliminary work of our group, we have demonstrated that LIBS can be used to distinguish gliomas from infiltrating border tissues [23]. However, the MFS in LIBS is still not widely understood and applied in biological samples. The full spectra or AS are most widely used signals in LIBS analysis. When detecting biological tissues, trace metal elements are

Biomedical Optics EXPRESS

easily affected by intraoperative hemorrhage and other effects, which brings elements in blood or body fluids to the sample. Meanwhile, non-metal elements such as C, H, O, and N are susceptible to be interfered by elements in the air. Therefore, the proposed MFS may highlight the changes of different tissues under the ablation of laser pluses. Tissues of 12 patients from four kinds of brain tumors (glioma, meningioma, hemangiopericytoma, and craniopharyngioma) were used in this research. Four types of tumors were identified as infiltrative tumors and non-infiltrative tumors. Compared with traditional machine learning data analysis methods, we introduced spiking neural network (SNN) in MFS data analysis. All calculations were conducted on a computer with an Intel Core i7-7700HQ CPU, windows 10 system and 16GB RAM. The SNN model was built on MATLAB 2016a.

2. Materials and methods

2.1. LIBS setup

The schematic of the experimental LIBS setup for brain samples measurement is illustrated in Fig. 1. There are already developed hand-held LIBS systems in other fields, which can be modified to meet the needs of intraoperative applications. As a pioneering theoretical verification study, we developed a desktop LIBS system to measure removal tissue. A He-Ne laser ($\lambda = 632.8$ nm) was used as pointing laser to indicate the optical path. Its red spot can indicate the position of the point to be measured, which makes it easy to tune the optical path. A flash-pumped Q-switched Nd: YAG laser ($\lambda = 1064$ nm, pulse frequency 1 Hz, pulse duration $\tau = 5$ ns, beam diameter Ø 6 mm, energy 40 mJ/pulse) was used to excite the sample's surface. The laser propagation direction was changed through three plane mirrors and finally focused on the sample surface by a convex lens with a focal length of 100 mm. The plasma radiation was collected into the fiber (Ø 600 μm) through a convex lens with a focal length of 36 mm. The outlet of optical fiber was connected to a two-channel spectrometer (AvaSpec 2048-2-USB2, Avantes). Spectral data collected by the spectrometer covers a range of 190 nm to 1100 nm with a resolution of 0.2~0.3 nm. External trigger used in the system included a photodetector and a digital delayer (SRS-DG535, Stanford Research System). When the photodetector detected the plasma radiation signal, the spectrometer was triggered by DG535 after a preset delay time. This preset spectral acquisition delay time was optimized to 1.29 μs to achieve the highest signal intensities. During the optimization of the delay time from the laser pulses disappeared to 1.40 μs, the molecular bands always present. The intensity of molecular band first raised and then felled with a highest intensity at 1.29 μs. The integration time of CCD was 2 ms. A three-dimensional motorized stage was used to adjust the focus position of the laser on the samples. Each shot was focused on a fresh position.

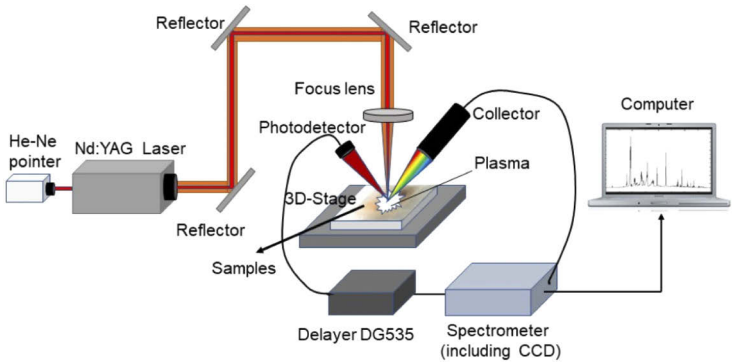

Fig. 1. Schematic of the LIBS setup.

Biomedical Optics EXPRESS

2.2. Sample collection

Human brain tumor tissues were obtained from department of pathology after routine tumor surgery. The patients gave written consent; the study was approved by the ethics committee at the Kunming Sanbo Brain Hospital (Kunming, China, April 2020).

Samples were collected from 12 brain tumor patients, including 4 glioma, 3 meningioma, 3 hemangiopericytoma, and 2 craniopharyngioma patients. Glioma, also known as neuroectodermal tumor, is the most common intracranial tumor, accounting for 40% to 50% of all brain tumors. Meanwhile, the glioma has the characteristic of infiltrating into the surrounding tissue, so the tumor boundary is not clear. All other known brain tumors have not shown the similar characteristic. Meningioma, hemangiopericytoma and craniopharyngioma are other three typical brain tumor types. Meningiomas are evolved from arachnoid cells or tissues not covered by meninges. Most of them are benign tumors, and a few have the possibility of malignant transformation. Hemangiopericytomas are true vascular tumors in the skull, which mostly occur in the cerebellum and are mostly malignant. Craniopharyngiomas are the most common congenital malignant tumors in the skull, which are more common in children and less common in adults. The tumor samples removed during the surgeries were sent to the pathology department to make FFPE sample blocks. Half of each tumor sample was used for pathological examination to determine the type of tumor, and the other half was prepared for LIBS detection. In this work, four kinds of brain tumors were identified as two types: the infiltrative and non-infiltrative tumors. Glioma has the characteristic of invasive growth, while this feature is not obvious in other brain tumors. So, the other three kinds of tumors are identified as one type. In order to ensure that the conclusions obtained are universal for other patients, we must guarantee the double-blindness between model training data and verification data. For each kind of tumor, samples from one patient were used to collect data for testing set. Samples from other patients were used to collect data for training set. Due to the different size of each tumor, the number of spectra available for each tumor was also different. After collecting the original spectra from each laser shot, each spectrum was accumulated from 10 laser shots according to the infiltrative or non-infiltrative type. The number of spectra obtained and the composition of data set are listed in Table 1. For training set, 355 spectra were collected in total, and for testing set, 123 spectra were collected.

Table 1. The composition of data set and tumor spectra number

Data set	Tumor types	Patient index	Laser shots	Spectra numbers
Training	Glioma	G1#	278	151
	Glioma	G2#	309	
	Glioma	G3#	923	
	Meningioma	M1#	431	204
	Meningioma	M2#	351	
	Hemangiopericytoma	H1#	458	
	Hemangiopericytoma	H2#	358	
	Craniopharyngioma	C1#	442	
	Glioma	G4#	440	44
Testing	Meningioma	M3#	284	79
	Hemangiopericytoma	H3#	280	
	Craniopharyngioma	C2#	226	

Biomedical Optics EXPRESS

3. Results and discussion

3.1. Formation mechanism of molecular fragment spectra (MFS) in brain tumors

Laser pulses were focused on the formalin-fixed paraffin-embedded (FFPE) samples of four kinds of brain tumors. Due to the laser ablation, trace amount of surface tissue was vaporized to generate plasma. During the plasma cooling process, we detected the light radiation, which was known as LIBS spectrum. The LIBS spectra of glioma, meningioma, hemangiopericytoma and craniopharyngioma are shown in Fig. 2. There are around 40 obvious lines in the LIBS spectra related to six molecular bands (three CN violet bands and three C_2 swan bands) and eight elements (four metal elements Ca, Mg, Na, K and four organic elements C, H, O, N). This indicated that all eight elements are present in the brain tumor samples. Although we have proved that metal elements like Ca and Mg could be used in the identification of glioma and infiltrative boundary tissues [23], such elements used in the identification of different brain tumors are still not perfect. As organic samples, the content of metal elements in biological tissues was very low. Meanwhile, the sample morphology of tissue was different from the conventional metal sample. Due to the lower hardness, which caused certain difficulties for laser excitation, some trace elements like Mg were not easy to detect in the spectra. Blood and body fluids brought by the intraoperative bleeding and other reasons might affect the content of trace metal elements like Na and K on the surface of the tumor. Therefore, although the intensities of Na and K showed significant differences in tumor samples, they were still not suitable to be used as diagnostic basis. The change of trace metal elements is usually a sign of tumor and healthy tissue [24], but the change of trace metal element contents between similar tumors still needs further study.

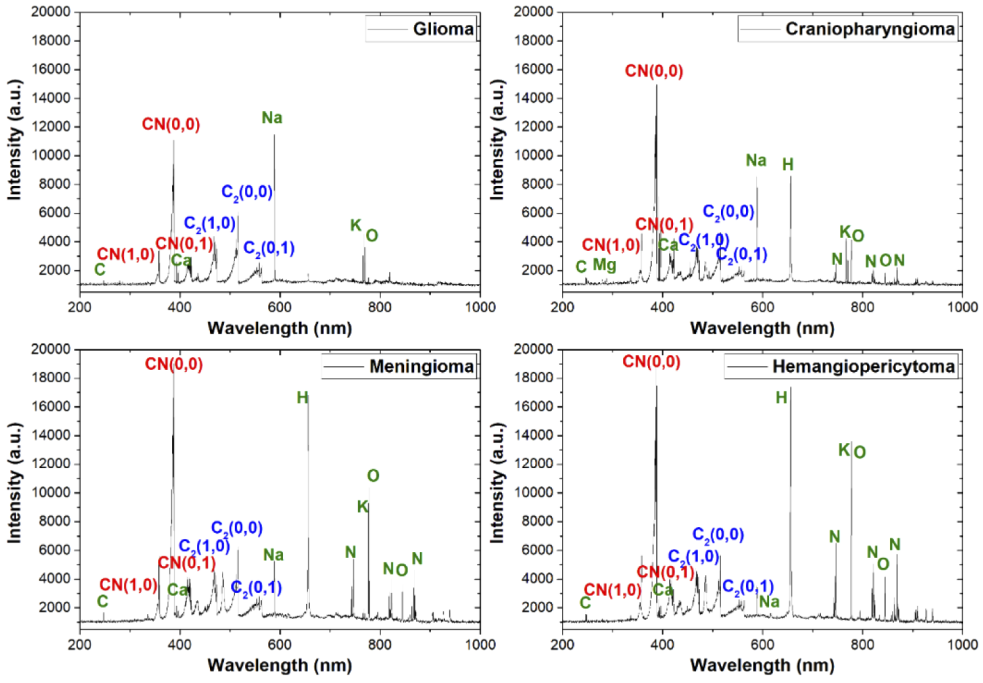

Fig. 2. The LIBS spectra of four kinds of brain tumors.

Some organic elements like C, H, O and N also took a main part in the spectra, especially the H, O and N. Compared with them, the C line at 274.8 nm was not obvious. These organic elements were not only the main component of biological tissues, but also the main part of environment air. All the experiments were done under standard atmospheric pressure in a conventional lab room,

Biomedical Optics EXPRESS

which was similar to the pathological testing environment. However, the main components in the air like N_2, O_2, H_2O and CO_2 could be also excited by the laser pulse. This would introduce interference in the LIBS spectra. The content of CO_2 is only 0.03% in the air, which makes C in the surrounding air contribute less to the spectra, while the intensity of the C line was lower than that of other organic element lines in the spectra. This may indicate that most of these element lines are contributed by air excitation.

In the LIBS spectra, element information is usually more abundant than molecular fragment information. Therefore, the LIBS spectrum is often used for the analysis of element content and difference in samples. Based on the above analysis, there should be some differences for brain tissue samples. The molecular fragments were particularly important in the identification of brain tumors based on LIBS spectra. Although the CN molecular fragments might have some elements such as N from the air environment, they were also produced by interacting with the elements in the sample under laser excitation. Therefore, MFS in the LIBS spectra reflected both the characteristics of the sample and the interaction process between the laser pulse and the brain tissue better. Although element lines like Na and K will have some influence on the plasma parameters and cause influence on the line intensities and profiles, the analyzed molecular bands profiles have less interference from this due to the widely different wavelength ranges. We normalized the spectra with the sum intensity of whole range during analysis to reduce the intensity bias. According to the reported review about LIBS in biomedical applications, the molecular bands are reliable marker, even though they don't represent the original proportion of C and N bonds exactly [25].

Six molecular bands can be recognized in Fig. 2, including violet bands CN (1,0), CN (0,0), CN (0,1) and Swan bands C_2 (1,0), C_2 (0,0), C_2 (0,1). Different from atomic lines, each band contains several peaks in its range. The detail information of these molecular bands is illustrated in Table 2.

Table 2. The MFS bands types and containing peaks

Types	MFS band	Central wavelength (nm)	Containing peaks (nm)
Violet CN	(1,0)	358	358.4
	(0,0)	384	384.6, 385.7, 386.5, 388.0
	(0,1)	417	414.8, 416.5, 417.6, 419.3
Swan C_2	(1,0)	470	467.3, 469.3, 470.9, 473.2
	(0,0)	516	509.2, 512.4, 516.0
	(0,1)	558	549.6, 553.4, 557.9, 562.8

According to the interaction between laser pulses and brain tumor tissues, the main formation mechanisms of MFS could be generalized into three categories, for instance, combination, reorganization and break. The detection process and formation mechanisms of MFS are illustrated in Fig. 3. The details of the experiments have been described in the Section 2. When the incident laser was focused on the tissue surface, the high-energy coupling into the sample in a short time would break the molecular bonds in the tissue. The formed plasma contained a lot of atoms, ions and molecular fragments. As Eq. (1) and (2) demonstrated, free atoms and ions will recombine to form molecular fragments. Biological tissue contains a large amount of C, which will generate a large amount of C atoms and C ions under high-energy laser excitation. Brain tumor tissue also contains a certain amount of N, but due to environmental factors, the main part of N atoms and ions may come from the excitation of N_2 in the air. The recombination of carbon atoms and ions forms the C_2 fragments, while the recombination of C and N atoms and ions forms the CN fragments. During the formation process of molecular fragments, light emission could be collected as MFS signals.

$$C + C \rightarrow C_2 \tag{1}$$

Biomedical Optics EXPRESS

$$C + N \rightarrow CN \tag{2}$$

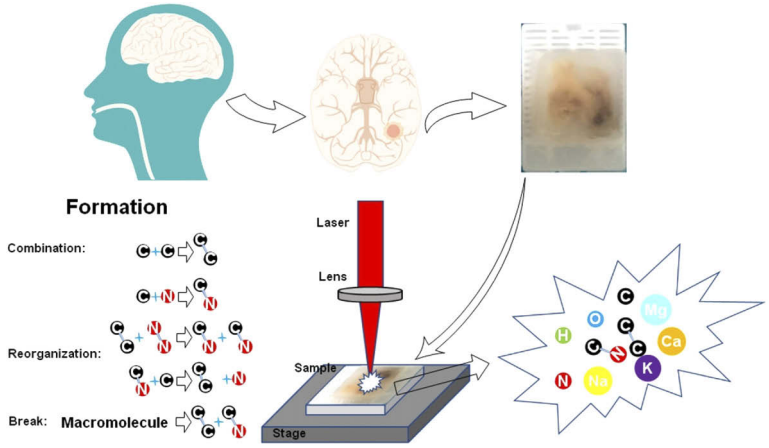

Fig. 3. The detection process and the formation of MFS.

If the laser pulses were not energetic to atomize all the chemical bonds of the ablated materials in the plasma, those molecular fragments that originate directly from the sample preserve their chemical-bond arrangements as in the solid sample [26]. In the plasma, these molecular fragments will generate secondary chemical bond breaks and reorganization, or they will recombine with atoms and ions, and then form new molecular fragments. Meanwhile, newly formed chemical bonds may also break again and recombine with other molecular fragments, atoms or ions. As demonstrated in Fig. 3, these two kinds of formation mechanisms of MFS can be recognized as reorganization, which represents the process of generating new molecular fragments from old molecular fragments. Exhaustively, the specific situations covered by this mechanism were shown in Eq. (3) to Eq. (8). Among them, the CN and C_2 fragments may be caused by the incomplete breakage of the original molecular bonds, or they may be generated by the first mechanism mentioned above. Most of the N_2 comes from the environment air around the plasma, but there may also be cases where the N-N bond in biological proteins is not broken sufficiently. As shown in Eq. (6), CH is a special case with element other than C and N. CH is the most common chemical bond in organic molecules, and it is also the chemical bond that is most likely to break incompletely under laser pulses ablation. The remaining CH will recombine with C to produce C_2.

$$C + N_2 \rightarrow CN + N \tag{3}$$

$$2C + N_2 \rightarrow 2CN \tag{4}$$

$$CN + C \rightarrow C_2 + N \tag{5}$$

$$C + CH \rightarrow C_2 + H \tag{6}$$

$$C_2 + 2N \rightarrow 2CN \tag{7}$$

$$C_2 + N_2 \rightarrow 2CN \tag{8}$$

$$Macromolecule \rightarrow CN + C_2 \tag{9}$$

The last formation mechanism of MFS is break. About this process, we have mentioned above when discussing the other two mechanisms. Biological tissue contains many different large molecules, including deoxyribonucleic acid (DNA), ribonucleic acid (RNA), protein, fat, et al. These molecules make up cells, and cells make up tissues. Under the action of the laser pulse

Biomedical Optics EXPRESS

ablation, the less stable chemical bonds are broken, but there may be other residual chemical bonds. Due to incomplete chemical bond breaks, CN and C_2 may be directly generated from macromolecules, as illustrated in Eq. (9). As mentioned, during the optimization of the delay time from the laser pulses disappeared to 1.40 μs, the molecular bands always present. Therefore, we assume that the mentioned cases all contribute to the intensities of the molecular bands. However, the degree of influence of each mechanism is different.

3.2. Data distribution and similarity judgment

For samples with obvious MFS differences, they can be directly distinguished by observation. Otherwise, the spectral data needs to be analyzed by intelligent data processing methods or statistical methods. As shown in Fig. 2, the MFS of these four kinds of brain tumors were too similar to identify by observation. Therefore, we calculated the sum intensity of each MFS band as spectral data and analyzed the data distribution and similarity first by principle component analysis (PCA). The original spectral data had multiple dimensions, and each dimension contained different amounts of information. It was difficult to characterize the information of the entire data by selecting several dimensions for analysis. As a commonly used dimensional reduction method for data in the field of spectral analysis, PCA can compress the variance information contained in the data into the first few dimensions by projecting the data into a less dimensional subspace through linear transformation. The variance of each principal component (PC) represents the proportion of original information they retain. Accumulating the variance of the first three PCs, the represented information accounted for more than 99% in this work. The score of each spectral sample on these three PCs can be used for clustering. The four kinds of brain tumor were distinguished as two types: infiltrative tumor (glioma) and non-infiltrative tumors (meningioma, hemangiopericytoma, and craniopharyngioma).

As Fig. 4(a) demonstrates, the two types of brain tumor could not be clustered into two categories. In order to analyze the data distribution and similarity further, different from the band data type, two new data forms have been developed, the peak data type and the ratio data type. The band and peak numbers are mentioned in Table 2. For the band data type, there are 6 bands and the bands intensities are used as inputs in the model. The band intensity is the sum of all peak intensities in this band. For the peak data type, there are 20 peaks in total and the peak intensities are used as inputs in the model. For the ratio data type, the ratios of band intensities are used as inputs in the model. Every two different bands can make a ratio and there are 15 ratios in total due to the mentioned 6 bands. The PCA clustering results of the peak data type and ratio data type MFS spectra were shown in Fig. 4(b) and 4(c).

It can be seen from the comparison of clustering results of the three data types that no matter what data type was adopted, the similarity of spectral data was relatively high. This situation is due to the similarity of the spectral band intensity itself, which was also consistent with the relatively similar characteristics among these tumors. However, this situation raised the requirements for the classification method in the identification process.

3.3. Quick identification by MFS combined with machine learning and brain-like computing methods

For accurate brain tumor identification based on MFS, 355 spectral samples (including 151 infiltrative tumor samples and 204 non-infiltrative tumor samples) were used to build the identification model, and 123 spectral samples (including 44 infiltrative tumor samples and 79 non-infiltrative tumor samples) from other patients were used to test the model. All three data types were used as input of the model and their identification results are demonstrated in Fig. 5, respectively. In recent years, machine learning algorithms and brain-like computing methods have been widely used in data processing. According to our experience in the spectral identification field [21,23], two conventional machine learning classifiers and the novel Spiking

Biomedical Optics EXPRESS

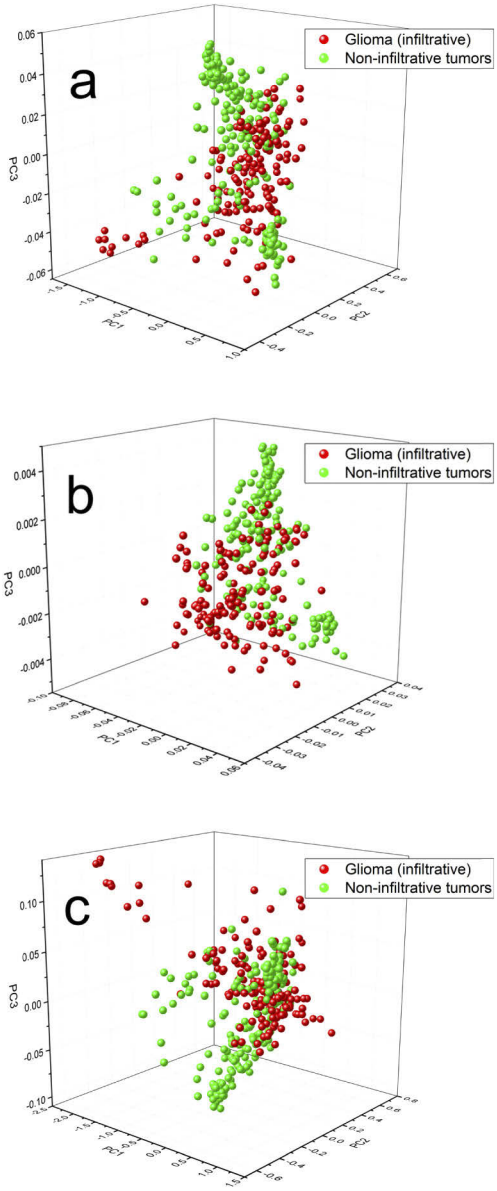

Fig. 4. The PCA cluster results of infiltrative and non-infiltrative tumors. (a: the band data type; b: the peak data type; c: the ratio data type)

Biomedical Optics EXPRESS

Neural Network (SNN) classifier were used to identify the different types of MFS data. The artificial neural network (ANN) was also used as a verification comparison of SNN to analyze the data. K-nearest neighbor (*k*-NN) is the most representative classification model that does not require training the model, and predicts based on the training set data. Support vector machine (SVM) is a very representative small sample training model, which works for both linear and nonlinear problems.

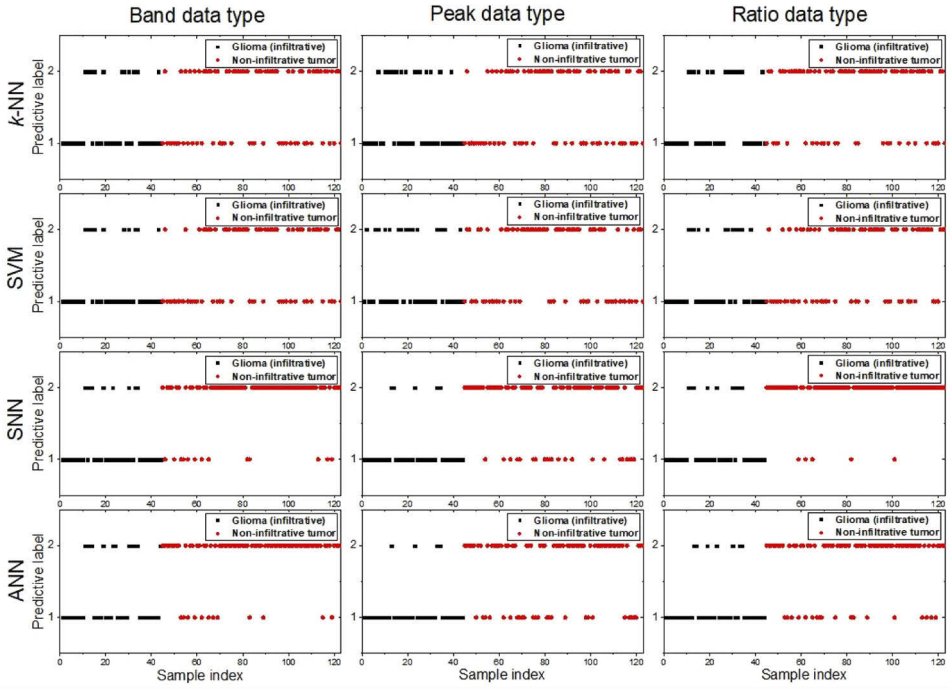

Fig. 5. The identification results of three data types by *k*-NN, SVM, SNN and ANN. (Predicted label 1: infiltrative tumor; predicted label 2: non-infiltrative tumor)

K-NN algorithm is a direct classification method to judge data categories based on distance. Distances of all sample points in multi-dimensional space were calculated. The category of each unknown data point is determined by the majority category of its nearest *k* known data points. In this work, the optimized *k* was set to 3. As shown in Fig. 6, the highest identification accuracy of *k*-NN classifier was 66.67%, which was related to the ratio data type. Such an identification accuracy rate could not provide effective help for intraoperative pathological diagnosis. SVM uses hyperplanes to split data category in multi-dimensional space. SVM can classify and identify both linearly separable and inseparable data. There is usually more than one hyperplane that can divide data categories in a multidimensional space. Selecting two parallel hyperplanes between the two categories of spectral data, linear separable SVM maximizes the interval between two hyperplanes to determine the maximum-margin hyperplane, which lies halfway between them. When the data is not linearly separable, a kernel function can be used to process the data and map the data to a high-dimensional space. Indivisible data in low-dimensional space will be separable in high-dimensional space, and then they can be distinguished according to the above steps. The punishment parameter *c* and the kernel parameter *g* were optimized by particle swarm optimization (PSO) algorithm. The corresponding SVM parameters are listed in Table 3. No matter what data format was used, the identification accuracy of SVM was not high enough, as shown in Fig. 6. Traditional machine learning methods had certain limitations in

Biomedical Optics EXPRESS

MFS data processing. The results of ANN model achieved a higher accuracy than *k*-NN and SVM. According to this, we suppose that the neural network models are more suitable for this identification problem than the traditional chemometrics. Furthermore, we propose to introduce the SNN classifier for identification of infiltrative and non-infiltrative brain tumors.

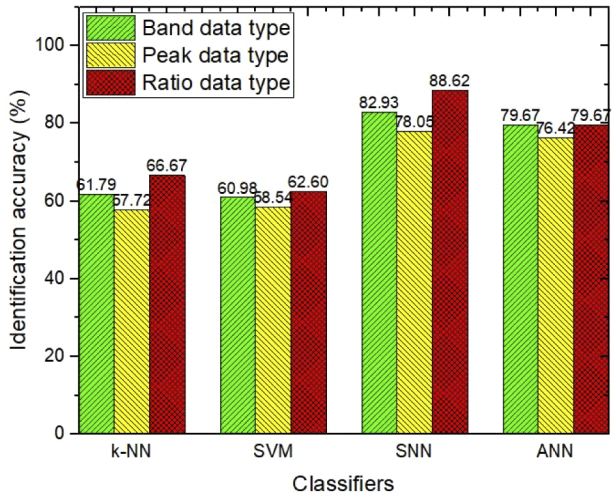

Fig. 6. The identification accuracy of infiltrative and non-infiltrative brain tumors.

Table 3. The corresponding parameters of the SVM classifiers

Data type	Punishment parameter (*c*) (nm)	Kernel function	Kernel parameter (*g*)
Band	1.5000	Gaussian	91.8292
Peak	100	Gaussian	7.8231
Ratio	0.7364	Gaussian	79.1539

As a third-generation neural network model, SNN achieves a higher level of biological neural simulation and is closer to the calculation process of the human brain [27]. During the data analysis, the human brain often shows much more powerful than conventional statistical methods. Therefore, ANN has been used as a powerful processing tool in LIBS field [28]. ANN is a widely parallel interconnected network composed of simple units with adaptability, and its organization can simulate the interactive reaction of biological nervous system to real-world objects. However, it takes a lot of time and computing power to build connections between dense neurons in the network. SNN may provide an efficient method of reasoning because the neurons in the network are sparsely activated. The most basic principle of conversion from ANN to SNN is that the firing frequency of pulse neurons should match the simulated activation value in ANN [29,30]. The built SNN model had only one hidden layer, same as the built ANN model, and the number of nodes contained in hidden layer was 40. The spiking neuron was training through the cuckoo search (CS) algorithm, which is a heuristic training method based on the cuckoo's parasitic brood behavior [31]. As illustrated in Fig. 5, compared with *k*-NN, SVM and ANN, the SNN classifier obviously performs better, especially with the ratio data type. Compared with ANN, the proposed SNN occupied CPU power by half. From the Fig. 6, we could see that the highest identification accuracy of infiltrative and non-infiltrative brain tumor achieved 88.62%. Such an accuracy has reached a higher level in the current study, and can provide auxiliary guidance for clinical oncology diagnosis. All three kinds of classifiers could finish the analysis process in 1

Biomedical Optics EXPRESS

s, which could meet the needs of rapid intraoperative diagnosis combined with the rapid LIBS measurement in 1 s. The proposed LIBS method doesn't need the complex sample preparation. During the surgery, the doctor only needs to cut the tumor off and put it on the sample stage before the detection. For all methods, this is an indispensable step, so we didn't count the time of this step for both our method and other methods.

As demonstrated in Fig. 6, the performance of the three data types under different identification algorithms expressed the same trend. The ratio data type had better adaptability for classification. By calculating the ratio between each two bands, the number of data features was expanded, and the MFS difference between infiltrative and non-infiltrative tumors was amplified. Since some peaks were from the same band, calculating each peak separately might ignore the relationship among them. Although calculating each peak separately could also increase the number of data features, its identification accuracy did not improve due to the lack of the correlation among the features. Meanwhile, the intensity of a single peak was susceptible to be interfered. The ratio data type could eliminate this interference to a certain extent, which could also explain why the peak data was the worst and the ratio was the best.

Traditional machine learning methods *k*-NN and SVM have similarly low-level recognition performances. The SNN model showed the best recognition ability. We explored the identification accuracies of the training set and the testing set further, and the results are listed in Table 4. Although the accuracies of testing set based on *k*-NN and SVM were only around 60%, the accuracies of training set were really high. Especially for SVM classifier with the input of peak data type, the accuracy of training data set achieved 97.46%. For these two classifiers, there were clear phenomena of overfitting. For SNN classifier, there was no such situation. In contrast, the identification results of the training set data were consistent with the testing set data, no matter which kind of data type was used as input.

Table 4. The identification accuracies of training and testing data set

Data type	*k*-NN accuracy (%)		SVM accuracy (%)		SNN accuracy (%)	
	Training set	Testing set	Training set	Testing set	Training set	Testing set
Band	90.42	61.79	90.70	60.98	78.31	78.05
Peak	89.86	57.72	97.46	58.54	82.54	82.93
Ratio	90.99	66.67	89.01	62.60	81.41	88.62

Traditional machine learning methods were prone to overfitting in the identification and analysis of MFS data, and the proposed SNN could effectively improve this problem.

4. Conclusions

This study is the first step towards introducing the MFS of LIBS technique in the clinically intraoperative identification of brain tumor. The MFS of LIBS was used alone in biomedical tissue identification for the first time. We conducted an in-depth analysis of the formation mechanisms of MFS in brain tissue, including three kinds of formation mechanisms: combination, reorganization and break. Combined with the proposed SNN brain-like computing method, the identification accuracy achieved 88.62% in 1 to 2 seconds. Three kinds of MFS data types were proposed in this work, and the ratio data type was proven to be the most suitable data type for identification, which was the least susceptible signal type to be interfered and could reflect sample characteristics more plentifully. The conventional machine learning methods *k*-NN and SVM performed not well due to the significant overfitting. As a third-generation neural network, SNN could solve this problem well.

Biomedical Optics EXPRESS

The results show that MFS-SNN is a potentially important technique for clinical brain tumor identification. On this basis, we will further conduct fresh tissue detection and research to promote the application of this technology.

Funding

National Natural Science Foundation of China (61775017); Graduate Technological Innovation Project of Beijing Institute of Technology (2019CX20026).

Acknowledgments

We sincerely thank the help from Prof. Michael Gaft for identifying the molecular lines. Geer Teng wants to thank Dr. Axin Fan for English language revision and encouragements during the inconvenient situation caused by COVID-19.

Disclosures

The authors declare no conflicts of interest.

References

1. F. Bray, J. Ferlay, I. Soerjomataram, R. L. Siegel, L. A. Torre, and A. Jemal, "Global Cancer Statistics 2018: GLOBOCAN Estimates of Incidence and Mortality Worldwide for 36 Cancers in 185 Countries," Ca-Cancer J. Clin. **68**(6), 394–424 (2018).
2. M. Giannakou, C. Yiallouras, G. Menikou, C. Ioannides, and C. Damianou, "MRI-guided frameless biopsy robotic system with the inclusion of unfocused ultrasound transducer for brain cancer ablation," Int. J. Med. Robotics Comput. Assist. Surg. **15**(1), e1951 (2019).
3. R. Galli, M. Meinhardt, E. Koch, G. Schackert, G. Steiner, M. Kirsch, and O. Uckermann, "Rapid Label-Free Analysis of Brain Tumor Biopsies by Near Infrared Raman and Fluorescence Spectroscopy—A Study of 209 Patients," Front. Oncol. **9**, 1165 (2019).
4. J. R. Busch, C. Jacobsen, N. Lynnerup, J. Banner, and M. Møller, "Expression of vasopressin mRNA in the hypothalamus of individuals with a diagnosis of schizophrenia," Brain Behav. **9**(9), e01355 (2019).
5. K. S. Nayanar, M. A. Krishnan, K. I. Mrudula, P. S. B. Thavarool, and S. Thiagarajan, "Frozen Section Evaluation in Head and Neck Oncosurgery: An Initial Experience in a Tertiary Cancer Center," Turk Patoloji Derg. **35**, 46–51 (2019).
6. A. J. Wright, G. A. Fellows, J. R. Griffiths, M. Wilson, B. A. Bell, and F. A. Howe, "Ex-vivo HRMAS of adult brain tumours: metabolite quantification and assignment of tumour biomarkers," Mol. Cancer **9**(1), 66 (2010).
7. C. Denkert, J. Budczies, W. Weichert, G. Wohlgemuth, M. Scholz, T. Kind, S. Niesporek, A. Noske, A. Buckendahl, M. Dietel, and O. Fiehn, "Metabolite profiling of human colon carcinoma – deregulation of TCA cycle and amino acid turnover," Mol. Cancer **7**(1), 72 (2008).
8. J. Sun, B. Li, C. Shu, Q. Ma, and J. Wang, "Functions and clinical significance of circular RNAs in glioma," Mol. Cancer **19**(1), 34 (2020).
9. M. Kazarian and I. A. Laird-Offringa, "Small-cell lung cancer-associated autoantibodies: potential applications to cancer diagnosis, early detection, and therapy," Mol. Cancer **10**(1), 33 (2011).
10. M. Wilson, N. P. Davies, M.-A. Brundler, C. McConville, R. G. Grundy, and A. C. Peet, "High resolution magic angle spinning 1H NMR of childhood brain and nervous system tumours," Mol. Cancer **8**(1), 6 (2009).
11. W. C. S. Cho, "Contribution of oncoproteomics to cancer biomarker discovery," Mol. Cancer **6**(1), 25 (2007).
12. V. Pirro, C. M. Alfaro, A. K. Jarmusch, E. M. Hattab, A. A. Cohen-Gadol, and R. G. Cooks, "Intraoperative assessment of tumor margins during glioma resection by desorption electrospray ionization-mass spectrometry," Proc. Natl. Acad. Sci. U. S. A. **114**(26), 201706459 (2017).
13. L. S. Eberlin, I. Norton, A. L. Dill, A. J. Golby, K. L. Ligon, S. Santagata, R. G. Cooks, and N. Y. R. Agar, "Classifying Human Brain Tumors by Lipid Imaging with Mass Spectrometry," Cancer Res. **72**(3), 645–654 (2012).
14. O. Uckermann, T. A. Juratli, R. Galli, M. Conde, R. Wiedemuth, D. Krex, K. Geiger, A. Temme, G. Schackert, E. Koch, G. Steiner, and M. Kirsch, "Optical Analysis of Glioma: Fourier-Transform Infrared Spectroscopy Reveals the IDH1 Mutation Status," Clin. Cancer Res. **24**(11), 2530–2538 (2018).
15. S. Marbacher, E. Klinger, L. Schwyzer, I. Fischer, E. Nevzati, M. Diepers, U. Roelcke, A.-R. Fathi, D. Coluccia, and J. Fandino, "Use of fluorescence to guide resection or biopsy of primary brain tumors and brain metastases," Neurosurg. Focus **36**(2), E10 (2014).
16. J. Desroches, M. Jermyn, M. Pinto, F. Picot, M.-A. Tremblay, S. Obaid, E. Marple, K. Urmey, D. Trudel, G. Soulez, M.-C. Guiot, B. C. Wilson, K. Petrecca, and F. Leblond, "A new method using Raman spectroscopy for in vivo targeted brain cancer tissue biopsy," Sci. Rep. **8**(1), 1792 (2018).

Biomedical Optics EXPRESS

17. M. Vendrell, K. K. Maiti, K. Dhaliwal, and Y.-T. Chang, "Surface-enhanced Raman scattering in cancer detection and imaging," Trends Biotechnol. **31**(4), 249–257 (2013).
18. S. J. Oh, S.-H. Kim, Y. B. Ji, K. Jeong, Y. Park, J. Yang, D. W. Park, S. K. Noh, S. G. Kang, Y.-M. Huh, J.-H. Son, and J.-S. Suh, "Study of freshly excised brain tissues using terahertz imaging," Biomed. Opt. Express **5**(8), 2837–2842 (2014).
19. R. Gaudiuso, N. Melikechi, Z. A. Abdel-Salam, M. A. Harith, V. Palleschi, V. Motto-Ros, and B. Busser, "Laser-induced breakdown spectroscopy for human and animal health: A review," Spectrochim. Acta, Part B. **152**, 123–148 (2019).
20. A. Taylor, N. Barlow, M. P. Day, S. Hill, N. Martin, and M. Patriarca, "Atomic Spectrometry Update: review of advances in the analysis of clinical and biological materials, foods and beverages," J. Anal. At. Spectrom. **33**(3), 338–382 (2018).
21. Q. Wang, G. Teng, X. Qiao, Y. Zhao, J. Kong, L. Dong, and X. Cui, "Importance evaluation of spectral lines in Laser-induced breakdown spectroscopy for classification of pathogenic bacteria," Biomed. Opt. Express **9**(11), 5837–5850 (2018).
22. F. Mehari, M. Rohde, R. Kanawade, C. Knipfer, W. Adler, F. Klämpfl, F. Stelzle, and M. Schmidt, "Investigation of the differentiation of ex vivo nerve and fat tissues using laser-induced breakdown spectroscopy (LIBS): Prospects for tissue-specific laser surgery," J. Biophotonics **9**(10), 1021–1032 (2016).
23. G. Teng, Q. Wang, H. Zhang, W. Xiangli, H. Yang, X. Qi, X. Cui, B. S. Idrees, K. Wei, and M. N. Khan, "Discrimination of infiltrative glioma boundary based on laser-induced breakdown spectroscopy," Spectrochim. Acta, Part B. **165**, 105787 (2020).
24. K. Cilliers, C. J. F. Muller, and B. J. Page, "Trace Element Concentration Changes in Brain Tumors: A Review," Anat. Rec. **303**(5), 1293–1299 (2020).
25. V. K. Singh and A. K. Rai, "Prospects for laser-induced breakdown spectroscopy for biomedical applications: a review," Lasers Med. Sci. **26**(5), 673–687 (2011).
26. M. Dong, G. C.-Y. Chan, X. Mao, J. J. Gonzalez, J. Lu, and R. E. Russo, "Elucidation of C_2 and CN formation mechanisms in laser-induced plasmas through correlation analysis of carbon isotopic ratio," Spectrochim. Acta, Part B. **100**, 62–69 (2014).
27. A. Taherkhani, A. Belatreche, Y. Li, G. Cosma, L. P. Maguire, and T. M. McGinnity, "A review of learning in biologically plausible spiking neural networks," Neural Networks **122**, 253–272 (2020).
28. X. Cui, Q. Wang, Y. Zhao, X. Qiao, and G. Teng, "Laser-induced breakdown spectroscopy (LIBS) for classification of wood species integrated with artificial neural network (ANN)," Appl. Phys. B: Lasers Opt. **125**(4), 56 (2019).
29. K. Kumarasinghe, N. Kasabov, and D. Taylor, "Deep learning and deep knowledge representation in Spiking Neural Networks for Brain-Computer Interfaces," Neural Networks **121**, 169–185 (2020).
30. P. S. Maciag, N. Kasabov, M. Kryszkiewicz, and R. Bembenik, "Air pollution prediction with clustering-based ensemble of evolving spiking neural networks and a case study for London area," Environ. Modell. Softw. **118**, 262–280 (2019).
31. H. Tran-Ngoc, S. Khatir, G. D. Roeck, T. Bui-Tien, and M. A. Wahab, "An efficient artificial neural network for damage detection in bridges and beam-like structures by improving training parameters using cuckoo search algorithm," Eng. Struct. **199**, 109637 (2019).